The subchalcogenides Ir$_2$In$_8$Q (Q = S, Se, Te): Dirac semimetal candidates with re-entrant structural modulation

Jason F. Khoury[1], Alexander J. E. Rettie[2,3], Iñigo Robredo[4,5], Matthew J. Krogstad[2], Christos D. Malliakas[1], Aitor Bergara[4,5,6], Maia G. Vergniory[5,7], Raymond Osborn[2], Stephan Rosenkranz[2], Duck Young Chung[2], and Mercouri G. Kanatzidis[1,2*]

[1]*Department of Chemistry, Northwestern University, Evanston, Illinois 60208, United States*
[2]*Materials Science Division, Argonne National Laboratory, Lemont, Illinois 60439, United States*
[3]*Electrochemical Innovation Lab, Department of Chemical Engineering, University College London, London WC1E 7JE, United Kingdom*
[4]*Donostia International Physics Center, Paseo Manuel de Lardizabal 4, 20018 Donostia-San Sebastian, Spain*
[5]*Condensed Matter Physics Department, University of the Basque Country UPV/EHU, 48080 Bilbao, Spain*
[6]*Centro de Física de Materiales, Centro Mixto CSIC-UPV/EHU, 20018 Donostia, Spain*
[7]*Ikerbasque, Basque Foundation for Science, E-48011 Bilbao, Spain*

Abstract

Subchalcogenides are uncommon compounds where the metal atoms are in unusually low formal oxidation states. They bridge the gap between intermetallics and semiconductors, and can have unexpected structures and properties because of the exotic nature of their chemical bonding, as they contain both metal-metal and metal-main group (e.g. halide, chalcogenide) interactions. Finding new members of this class of materials presents synthetic challenges, as attempts to make them often result in phase separation into binary compounds. We overcome this difficulty by utilizing indium as a metal flux to synthesize large (mm scale) single crystals of novel subchalcogenide materials. Herein, we report two new compounds Ir$_2$In$_8$Q (Q = Se, Te) and compare their structural and electrical properties to the previously reported Ir$_2$In$_8$S analogue. Ir$_2$In$_8$Se and Ir$_2$In$_8$Te crystallize in the *P*4$_2$/*mnm* space group and are isostructural to Ir$_2$In$_8$S but also have commensurately modulated (with q-vectors q = 1/6a* + 1/6b* and q= 1/10a* + 1/10b* for Ir$_2$In$_8$Se and Ir$_2$In$_8$Te, respectively) low temperature phase transitions, where the chalcogenide anions in the channels experience a distortion in the form of In-Q bond alternation along the *ab* plane. Both compounds display re-entrant structural behavior, where the supercells appear on

cooling but revert to the original subcell below 100 K, suggesting competing structural and electronic interactions dictate the overall structure. Notably, these materials are topological semimetal candidates with symmetry-protected Dirac crossings near the Fermi level, and exhibit high electron mobilities (~1500 cm^2 V^{-1} s^{-1} at 1.8 K) and moderate carrier concentrations (~10^{20} cm^{-3}) from charge transport measurements. This work highlights metal flux as a powerful synthetic route to high quality single crystals of novel intermetallic subchalcogenides.

Introduction

Among the several broad classes of materials, chalcogenides and intermetallics are prominent, but very different from each other. The former are generally semiconductors, with bonding that is a mix of both covalent and "salt-like" ionic character depending on the metals. These materials are conventional and tend to follow the so-called 8-N octet rule, and because of the ionic character of the bonding we consider the metal atoms to be oxidized with the electrons fully transferred to the chalcogen atoms. Conversely, intermetallics do not obey the standard 8-N rule, as they have metallic properties with very high carrier concentrations and bonding that is a mixture of covalent and metallic. Metal atoms in intermetallics that form metal-metal bonds are thought to have very low or zero oxidation states. Hybrid compounds that combine the bonding features of chalcogenides (or halides) and intermetallics are rare.[1-2] In such hybrids, we expect the metals to have both covalent bonds to the chalcogen atoms, as well as metal-metal bonds to each other with low oxidation states and only partially oxidized character.[3] These hybrid compounds are therefore very metal rich and have technically subvalent metals.

Some known subchalcogenides and subhalides have attracted great interest as topological materials, as their exotic bonding motifs have led to unusual surface states and Fermi surface topologies, such as the cases of the weak topological insulator $Bi_{14}Rh_3I_9$ and Weyl semimetal candidate $Sn_2Co_3S_2$.[4-10] Other subchalcogenides exhibit charge density wave (CDW) behavior or superconductivity, as their lower dimensionalities facilitate electron-electron interactions that

lead to these phenomena.[7-8, 11] These discoveries, and the promise of new chemistry and physics in these types of materials, motivate further studies into their synthesis pathways.

Chemically, subchalcogenides and subhalides derive from an intermetallic framework that has been partially oxidized to have metallic and ionic regions. The comparatively electronegative halide and chalcogenide ions act as electron density acceptors from the metal atoms. Ruck and coworkers have done extensive work into developing methodology for ternary bismuth subhalides.[12-17] The synthetic methodology and bonding behavior of subchalcogenides, however, is not fully understood. Many reported examples can form polar covalent bonds between the chalcogen and metal atoms while still forming a partially oxidized, metal-rich structure, such as the cases of binary Ta_6S, Zr_9S_2, and $Nb_{14}S_5$.[18-22] Ternary and multinary subchalcogenides promise an even greater degree of structural diversity with novel structure types and metal-rich substructures.[11, 23-25]

The main challenge with the development of new complex subvalent chalcogenides, however, has been in their synthesis.[20, 26-28] Whereas flux-based methodologies for new materials are known for chalcogenides and intermetallics, it is especially challenging to find proper synthetic conditions that more reliably favor paths to subvalent chalcogenides.[24-25, 29-33] This is because of the tendency to phase separate into classical intermetallics and chalcogenides. Therefore, development of the metal flux as a tool for novel subchalcogenide synthesis is important since it also advances the synthesis science of this materials class.

Indium metal fulfills this need because it is a suitable reactive flux for chalcogen atoms as well as heavy metals from the platinum group (e.g. Ir, Pt, Rh, Pd, Ru, Os). Since indium is much less electronegative than the chalcogens and platinum group metals, it can reduce them and act as a bridging element in forming metal-rich intermetallic chalcogenide frameworks. By

utilizing this approach, we can synthesize new subchalcogenides by altering the identity and composition of the reagents. In doing so, we advance the synthetic methodology of an underexplored class of materials which may harbor new or surprising physical properties.

We successfully applied this methodology to form a set of new subchalcogenide materials from an indium flux, the compounds Ir_2In_8Q (Q = S, Se, Te). In this work, we describe the synthesis methodology, crystallography, phase transitions, and charge transport measurements of Ir_2In_8Se and Ir_2In_8Te, and compare them to the previously reported Ir_2In_8S.[34] Both compounds have the same structure type as Ir_2In_8S, crystallizing in the $P4_2/mnm$ space group at room temperature, where they exist as three-dimensional (3D) polyhedral frameworks with chalcogenide ions in channels along the c axis. Density functional theory and group theoretical analysis shows that Ir_2In_8Se and Ir_2In_8Te are also Dirac semimetals (like Ir_2In_8S) and this is corroborated by their moderate carrier concentrations ($\sim 10^{20}$ cm^{-3}) and high electron mobilities ($\sim 10^3$ cm^2 V^{-1} s^{-1} at 1.8 K). Ir_2In_8Se and Ir_2In_8Te undergo commensurately modulated phase transitions at low temperature, but surprisingly both structures revert to their original subcells below ~100 K. The sulfide analogue, in comparison, does not have supercell ordering, but a sudden reduction in diffuse scattering below 230 K, indicating the absence of local distortions in the structure below that temperature. Most prominent topological materials to date have been found in the pool of already known compounds with similar crystal structures. The successful synthesis of Ir_2In_8Q compounds using an indium metal flux reaction route, however, highlights a new family of topological semimetal candidates available for investigation.

Experimental Details

Reagents. All reagents were used as obtained: Ir powder (99.5%, American Elements), In teardrops (99.999%, Plasmaterials), Sulfur pieces (99.998%, Sigma Aldrich), Selenium pieces (99.99%, American Elements), and Tellurium pieces (99.999%, Plasmaterials).

Synthesis. For Ir_2In_8Se and Ir_2In_8Te, Ir (0.05 mmol, 0.0961 g), In (20 mmol, 2.2964 g), and either Se (2 mmol, 0.1579 g) or Te (2 mmol, 0.2552 g) were loaded into alumina crucibles. For Ir_2In_8S, the molar ratios were different, as Ir (1 mmol, 0.1922 g), S (0.5 mmol, 0.0163 g), and In (20 mmol, 2.2964 g) were required to form the desired product with minor amounts of $IrIn_3$ forming as a side product in some reactions. In all cases, a 100-mesh stainless steel filter was placed on top of the alumina crucibles, and a small piece of alumina tubing was placed on top of the filter as a counterweight. The crucible, filter, and tubing were loaded into 18 mm fused silica tubes and sealed under vacuum at ~3 x 10^{-3} mbar, and divots were made in the tube with the flame after sealing to ensure that the set up stayed in place.[35] The reactions were heated to 1000 ℃ in 12 h, held there for 24 h, and cooled to 650 ℃ in 24 h. After being held at 650 ℃ for a few hours, the tubes were removed from the furnace and immediately centrifuged to remove excess indium flux. Residual indium on the surface of the crystals was removed by etching in dilute (10% by weight) HCl for 2-3 hours, and then the crystals were filtered and washed with water and acetone. The crystals are stable in water, acetone, and dilute HCl for at least 2-3 days. The total yields for these reactions range from 50-75% by weight depending on the limiting reagent.

Single Crystal X-ray Diffraction. Crystals of Ir_2In_8Q were adhered to a glass fiber with super glue. Single crystal x-ray diffraction was performed at ~298 K on a Bruker-APEX II CCD diffractometer with MoKα radiation (λ = 0.71073 Å). The data for the subcells were integrated using SAINT-v8.38A and the multi-scan absorption correction was applied using SADABS.[36] The subcells were solved with intrinsic phasing in the SHELXT software package, and refined

with SHELXL by the Least Squares method.[37] The superstructures were refined using JANA2006 software.[38] The crystallographic information for the structures can be found in Tables 1-2. Additional crystallographic information can be found in the supporting information.

Scanning Electron Microscopy (SEM) and Energy Dispersive Spectroscopy (EDS). Scanning electron microscopy and semi-quantitative energy dispersive spectroscopy were performed with a Hitachi S-3400 scanning electron microscope supplied with a PGT energy-dispersive x-ray analysis attachment. EDS measurement parameters were 25 kV, 70 mA probe current, and the acquisition time for each measurement was 60 s. EDS data were taken from flux-grown single crystals of Ir_2In_8Q with well-defined faces (Figures S1-2).

Density Functional Theory (DFT) Calculations. Band structure calculations were performed using Density Functional Theory (DFT) as implemented in the Vienna Ab initio Simulation Package (VASP).[39-42] The interaction between ion cores and valence electrons was treated by the projector augmented-wave method (PAW), the generalized gradient approximation (GGA) for the exchange-correlation potential with the Perdew-Burke-Ernkzerhof for solids parametrization and spin-orbit coupling (SOC) was taken into account by the second variation method.[43-45] A Monkhorst-Pack k-point grid of ($8 \times 8 \times 8$) for reciprocal space integration and 500 eV energy cutoff of the plane-wave expansion have been used.

Charge Transport Properties. Temperature dependent resistivity and Hall effect measurements on single crystals of Ir_2In_8Q with approximate dimensions of $1 \times 1 \times 0.3$ mm^3 were conducted on a Quantum Design Dynacool Physical Property Measurement System (PPMS) with a temperature range between 1.8 and 300 K. Resistivity was measured in a 4-point collinear geometry and the Hall effect measured using two Hall voltage contacts placed perpendicular to the axis of current flow. The magnetic field was applied perpendicular to the

axis of current flow from -9 to +9 T, and temperature and field were cycled multiple times to confirm data reproducibility. Electronic conductivity and Hall effect measurements were performed simultaneously on the same sample for Ir_2In_8Se and Ir_2In_8Te. To ensure stable, Ohmic contact, Au metal pads were thermally evaporated on the samples and Au wires were attached with silver paste (Dupont 4929N).

Heat Capacity. Heat capacity (C_p) was measured using a Quantum Design Dynacool PPMS between 1.8 and 300 K. Apiezon N grease was used to couple samples to the heat capacity stage. Data were collected on warming.

Synchrotron X-ray Scattering. Temperature-dependent diffuse scattering data were collected from single crystals at Sector 6-ID-D at the Advanced Photon Source using an incident wavelength of 0.14255 Å and a Dectris Pilatus 2M detector with a 1 mm-thick CdTe sensor layer. Data were collected from 30 to 300 K with the sample cooled using He gas below 100 K and N2 gas above 100 K. Crystals were affixed to Kapton capillaries using a binary epoxy. During measurements, the sample was rotated at 1° per second over 365°, with images read out every 0.1 s. Three sets of rotation images were collected at each temperature to fill in gaps between detector chips, with a 15° ω-rotation performed between each rotation scan to allow for the masking of Compton scattering artifacts without losing coverage. The resulting images were stacked into a three-dimensional array, oriented using an automated peak search algorithm, and transformed into reciprocal space coordinates using the software package CCTW, allowing the structure factor S($\mathbf{Q}$) to be determined over a large range of $|Q| \sim +/- 15$ in all directions.[46] NeXpy software was used for analysis.

Results and Discussion

Synthesis. The metal flux has proven to be a powerful tool for growing large (mm scale), high quality single crystals that are suitable for property measurements.[24-25, 32, 47-52] Here we utilized liquid indium to dissolve both iridium metal and the chalcogen of interest to access three different isostructural compounds Ir_2In_8Q as large crystals, and thereby demonstrate the potential to synthesize subchalcogenides with this method. Scanning electron microscopy (SEM) and semi-quantitative energy dispersive spectroscopy (EDS) for the newly reported Ir_2In_8Se and Ir_2In_8Te can be seen in Figures S1-2. In the case of the selenide and telluride analogue, the ratio of Ir:In:Q was 0.5:20:2, and the yield was 70-75% based on the limiting reagent iridium. Altering the ratios of iridium with Q (selenium or tellurium) did not significantly alter the yield of the ternary product, and no other compounds were observed. Lowering the temperature from 1000 °C to 800 °C also did not change the identity of the final product, but the crystals tended to be smaller and in lower yield. For the sulfide, the Ir:In:S ratio was 1:20:0.5, with a lower yield of 50-60% and a noticeably larger amount of secondary $IrIn_3$ crystals. From one perspective, we may consider the Ir_2In_8Q to be a chemical reaction adduct between two equivalents of $IrIn_3$ and one of In_2Q.

Structure. Ir_2In_8Se and Ir_2In_8Te crystallize in the same structure type as Ir_2In_8S in the $P4_2/mnm$ space group. Crystallographic information, as well as selected bond distances, are listed in Tables 1-2 and Tables S1-12. The structure is a 3D framework assembled by eight-coordinate $IrIn_8$ polyhedra with chalcogenide anions found in the channels along the c axis, Figure 1. The $IrIn_8$ polyhedra (Figure 2) are distorted bicapped trigonal prisms that are corner sharing along the a and b axes but alternate between corner and edge sharing along the c axis, resulting in the tetragonal nature of this compound. An In-In bond with nearly identical lengths for the sulfide (2.6843(19) Å) and selenide (2.6806(18) Å), but longer for the telluride (2.712(3) Å) connects

the edge-sharing polyhedra along the c axis (see Table 2). The In-In bond in Ir_2In_8Q is shorter than the In_2^{2+} dimer in InS (2.7624(4) Å). The structure itself has similarities to the binary intermetallic $IrIn_3$, as it also crystallizes in the $P4_2/mnm$ space group and has bicapped trigonal prismatic $IrIn_8$ polyhedra. However, the polyhedra in $IrIn_3$ are face-sharing along the ab plane and there are no large, clearly defined channels like with Ir_2In_8Q. The similarities between these structures highlight the stable bonding preferences between Ir and In in an In-rich environment, which can tolerate a small amount of oxidation by the chalcogenide anions to form dimensionally reduced subchalcogenides with an open polyhedral framework. An analysis of the Fourier difference maps for all three structures show consistent features, such as a noticeable hole density on the indium atoms of the structure as well as minor hole density on the iridium atoms. Due to the lower electronegativity of indium, it likely donates electrons to the chalcogen atoms and, to a lesser extent, iridium, making the Ir-In polyhedral network have an overall positive charge to compensate the chalcogenide anions in the channels along the c axis. Given the corner and edge-sharing connectivity of the $IrIn_8$ polyhedra, as well as the In-In bonding along the c axis, there is likely an overall delocalization of the positive charge along the framework, allowing for the semimetallic behavior shown in the electronic structure and charge transport sections below.

By changing Q in the structure, the angles of the connecting polyhedra surrounding the chalcogenide anions in the channels are distorted. For example, the In3-In3-In3 angle changes from 82.737(14)° to 84.617(11)° to 86.533(11)° for the sulfide, selenide, and telluride analogues, respectively. The polyhedral distortion is caused by the size differences of the Q^{2-} anions, as we will see below they indirectly modify the electronic structure to cause significant changes in the physical properties of each compound. These distortions change with temperature and manifest

as anomalous features in the temperature-dependent resistivity of each compound, as the sulfide had a kink at 230 K, the selenide had a change in slope at 203 K, and the telluride had a large peak that began at 150 K and ended at 110 K (see charge transport section below), and these features are correlated with structural transitions in all three materials.

Re-entrant Structural Modulation. Because of the unusual electrical discontinuities (presented below), we performed single-crystal diffuse x-ray scattering measurements at Sector 6-ID-D at the Advanced Photon Source at Argonne National Laboratory. Scattering data allowed us to observe changes in weak Bragg reflections (supercells, incommensurate modulation, etc.) as well as changes in diffuse scattering along several planes, coincident with the presence of local distortions in the structure that otherwise were not detectable via laboratory single-crystal x-ray diffraction. Single crystals of Ir_2In_8Q were measured at temperatures between 30 K and 300 K (Figure 3). We see that the resistivity kink in Ir_2In_8S at 230 K is associated with a change in diffuse scattering, as there are multiple discrete scattering rods at and above the kink temperature that disappear below it (see Figure 3A). These effects reflect structural distortions occurring on cooling and are likely caused by movement of the indium atoms connecting the polyhedra. In particular, the source of the local distortion in Ir_2In_8S is likely movement of the In(5) atom, as there is noticeable hole density on both sides of it in the Fourier difference map of the structure at 299 K.

In contrast to Ir_2In_8S, Ir_2In_8Se and Ir_2In_8Te have three separate structural regimes: A higher temperature regime (203 – 300 K for Ir_2In_8Se, 150 – 300 K for Ir_2In_8Te) where Bragg reflections as well as diffuse scattering are present, a medium temperature regime (110 – 203 K for Ir_2In_8Se, 100 – 150 K for Ir_2In_8Te) with supercell ordering, and a low temperature regime (< 100 K) with only Bragg reflections clearly observable (Figure 3B-C and Figures S3-4). The

temperature ranges of supercell ordering in the selenide and telluride analogues are consistent with the transport anomalies and heat capacity data shown below. The appearance and disappearance of the modulation, known as re-entrant behavior, is a rare feature that has only been observed in one other system, to our knowledge, and could potentially be the result of CDW behavior in these materials.[53] Ir_2In_8Se and Ir_2In_8Te also have noticeable hole density near the In(5) atom in their Fourier difference maps in the 299 K subcells, indicating that the source of diffuse scattering in all three structures results from distortions of the $IrIn_8$ polyhedra by movement of the indium atoms. The distortion of these indium atoms also would distort the position of the Q atom in each structure, explaining their relatively elongated anisotropic displacement parameters (ADPs) at 299 K (see supporting information).

The supercell orderings had the q-vectors q = 1/6a* + 1/6b* and q= 1/10a* + 1/10b* for Ir_2In_8Se and Ir_2In_8Te, respectively, indicating 6x6 and 10x10 supercells along the *ab* plane. By identifying temperatures where the supercell reflections are at their strongest in both analogues, we solved their commensurately modulated structures using laboratory single-crystal x-ray diffraction, as seen in Figures 4-6 and Tables S13-S18. Both supercells are diagonally oriented along the *ab* plane and adopt the *Pm*($\alpha\beta$0)0 superspace group, where the position of the chalcogenide atoms along the *ab* plane is modulated (Figure 4). The distortion reflects In-Q bond alternation along the *ab* plane, with bond lengths ranging from ~2.8 – 4 Å (Figure 5). Because of the additional indium chalcogenide interactions, the square planar geometry in the subcell turns into 5 and 6-coordinate In-Q environments in the supercell, where the extra In atoms are along the axial plane (Figure 6). The resultant structural modulation is likely the coalescence of the local distortions that caused the noticeable diffuse scattering in the high temperature subcells of Ir_2In_8Se and Ir_2In_8Te to become supercell ordering. The movement of the In(5) and Q atoms in

each structure occurs in a sinusoidal pattern, where they distort to become closer together and then farther apart, creating the modulated supercells for each structure. It is not obvious why Ir_2In_8Se and Ir_2In_8Te have different commensurate supercells (6x6 as opposed to 10x10, respectively), but it is likely attributable to differences in size and polarizability of their respective chalcogen atoms.

The origin of the re-entrant behavior in both structures is not fully understood, but may derive from competing structural and electronic distortions, and the charge transport data of Ir_2In_8Te suggests that an energy gap could be opening because of the commensurately modulated supercell. An energy gap, coincident with a modulated structural phase transition, resembles a Peierls distortion that often leads to CDW behavior, where electronic instabilities cause periodic modulations of conduction electrons that lead to structural transitions.[54] If the re-entrant modulation in both structures is the result of competing structural and electronic effects, the amount of thermal energy in the system dictates which effect is stronger, explaining why the supercells only exist in distinct temperature windows.

Electronic Structure. The calculated electronic band structures of Ir_2In_8Se and Ir_2In_8Te are shown in Figure 7A-B. Both band structures have two tilted crossings along the $\Gamma - Z$ direction below the Fermi level (8.2 and 9.8 meV below for the left and right crossing of Ir_2In_8Se, 11.0 and 6.3 meV below for the left and right crossing of Ir_2In_8Te). The crossings are like the isostructural Dirac semimetal candidate Ir_2In_8S, which had the same two tilted (e.g. type-II) crossings 25 and 40 meV above the Fermi level.[34] It is surprising that Ir_2In_8Se and Ir_2In_8Te have their two Dirac crossings below the Fermi level but Ir_2In_8S has the same two crossings above it, since all three should have identical electron counts. The movement of these two crossings below the Fermi level is likely attributable to distortion of the $IrIn_8$ polyhedra by the

larger chalcogenide anions, altering the dispersity and location of the bands. Partial density of states (PDOS) plots show that the Ir and In orbitals are the dominant contributors for all of the bands, with the chalcogenide atoms contributing very little to the electronic structure (Figure S5). To probe the topological nature of these crossings in Ir_2In_8Se and Ir_2In_8Te and compare them to Ir_2In_8S, we utilized the CheckTopMat application from the Bilbao Crystallographic Server (BCS) and computed the irreducible representations of the occupied bands between the high symmetry points Γ and Z. These calculations confirm that the crossings in both the selenide and telluride are also protected by symmetry, confirming their topological behavior (Figure 7C-D).[55] For the two band crossings observed along the line, Λ, there are two additional crossings due to time reversal symmetry, leading to four total crossings when considering the $\Gamma - Z$ and $\Gamma - -Z$ directions. Like with Ir_2In_8S, the band structures are similar to the Dirac semimetal Na_3Bi but with four total crossings instead of two.[56]

To understand how these crossings are protected in Ir_2In_8Se and Ir_2In_8Te and compare them to Ir_2In_8S, we can compute the irreducible representations below the Fermi level for the high symmetry line Λ along the $\Gamma - Z$ direction.[57-59] Since the selenide and telluride compounds are isostructural to the sulfide analogue, the presence of the 4_2 screw axis again differentiates the irreducible representations in the band structure, preventing their hybridization. If this screw axis were to be perturbed by breaking the symmetry of the structure, the bands would be allowed to mix due to hybridization, opening an energy gap. Hybridization potentially opening a gap is a salient point to consider given the low temperature modulated structures in Ir_2In_8Se and Ir_2In_8Te, as it is possible that the lower symmetry $Pm(\alpha\beta0)0$ superspace group results in gap formation in the electronic structure, an idea supported in the charge transport measurements section below. We have also computed the Fermi velocities of the tilted Dirac crossings in both compounds and

shown that they are comparable in magnitude to Ir_2In_8S, as seen in Table S19 in the supporting information. Ir_2In_8S had a Fermi velocity ten times larger than in the known Dirac semimetal Na_3Bi along the z direction, and this may contribute to high carrier mobility and magnetoresistance in high-quality crystals of Ir_2In_8Se and Ir_2In_8Te.[56]

Charge Transport. The four-probe resistivity (ρ) data for both heating and cooling cycles for Ir_2In_8Q are shown in Figure 8. All transport measurements were performed with current applied along an arbitrary axis. Ir_2In_8S displays metallic behavior with a clear kink in the resistivity at 230 K, coincident with the change in diffuse scattering mentioned above, as the local distortions in the structure suddenly disappear. At higher temperatures above the transition, there is hysteresis in the measurement, which could be a function of the local distortions reappearing in the structure and affecting the bonding between polyhedra. Ir_2In_8Se is also metallic but there is a change in slope that occurs at 203 K, coincident with the onset of supercell ordering in the structure. The supercell ordering disappears at 110 K, but any apparent change in resistivity is too subtle to notice from the measurement on either the cooling or warming cycle. Ir_2In_8Te, in comparison to the other two analogues, has the most striking resistivity behavior of the three. It also behaves in metallic fashion initially, with the resistivity decreasing with decreasing temperature, but at 150 K the resistivity increases sharply and reaches a maximum at 125 K. After reaching its peak, it decreases sharply until about 110 K where the resistivity has another change in slope. These electrical features are also correlated with the structural data presented above, as supercell Bragg reflections begin at 150 K, persist until 115 K, and have disappeared by 100 K (Figure 3).

It is a curious result that both Ir_2In_8Se and Ir_2In_8Te have supercell ordering, but the manifestation of that ordering in their electrical behavior is quite different. The larger supercell

of the telluride compound may be linked to more pronounced electronic instabilities, which presumably opens an energy gap in the Fermi surface of the structure and explains the change in electrical behavior from metallic to semiconducting.[60-64] The presence of an energy gap in Ir_2In_8Te also leads to further questions about the topological character of the supercell compared to the subcell, as it is possible that the gap formed could be topologically nontrivial (i.e. a topological insulator). In addition, if the electronic instability in Ir_2In_8Te is indeed a CDW, then Ir_2In_8Te could be a so-called Axion insulator candidate material, a correlated topological phase that occurs when a CDW arises in a topological semimetal.[65]

Variable-temperature Hall effect data for Ir_2In_8Se and Ir_2In_8Te are shown in Figure S6. The Hall resistivity for both compounds is negative, suggesting that electrons are the majority carrier type. Ir_2In_8Se and Ir_2In_8Te go from linear to nonlinear Hall resistivity below their characteristic supercell ordering temperatures (203 and 150 K, respectively). In all three cases, the degree of nonlinearity becomes more severe as the temperature decreases down to 1.8 K. Even when the supercell ordering has disappeared at low temperatures for the selenide and telluride analogue, the Hall resistivity at low temperatures is still nonlinear. The low temperature (< 50 K) Hall resistivity data for Ir_2In_8Se were fitted with a two-band model to approximate both electron and hole mobilities and carrier concentrations (Figure 9 and Figure S6).[66] However, for Ir_2In_8Te, a single-band approximation had to be used because the data could not be fit to a two-band model.

The carrier concentrations of the selenide and telluride compounds, seen in Figure 9, are approximately 10^{20} cm^{-3}. Ir_2In_8Te has a spike in its carrier concentration at the same temperature as its resistivity peak (150 K), and this is likely an artifact of the proposed energy gap opening in the structure, similar to the behavior seen in $ZrTe_5$ when the Fermi level moves through the band

gap.[67] The electron carrier mobility values at 1.8 K are high for Ir_2In_8Se and Ir_2In_8Te (~1400 and 1250 cm^2 V^{-1} s^{-1}, respectively), but not as high as in Ir_2In_8S (~10^4 $cm^2V^{-1}s^{-1}$).[34] Ir_2In_8Se also had hole mobilities of ~900 and ~700 $cm^2V^{-1}s^{-1}$ at 1.8 and 50 K, respectively, along with noticeably lower hole carrier concentrations of ~5 x 10^{19} and ~7 x 10^{18} cm^{-3} at those same respective temperatures. The higher mobility in Ir_2In_8S compared to the other two analogues is attributable to a higher residual resistivity ratio (RRR, $\rho_{300 K}/\rho_{1.8 K}$) in those measured crystals, suggesting that crystal quality and orientation are important factors in influencing the carrier mobility for all three compounds. The magnetoresistance (MR) data in Figure S7 corroborate the high mobilities of these structures, as both Ir_2In_8Se and Ir_2In_8Te have high MR% values of 275% and 500% at the same conditions, respectively. Since transverse magnetoresistance is proportional to the mobility of a material (MR = 1 + $(\mu B)^2$), the fact that Ir_2In_8S has a much higher MR% is in line with its significantly larger mobility than the other two analogues.

Heat Capacity. The heat capacity for these samples of Ir_2In_8Q shows standard Debye behavior except that each analogue has a noticeable bump or kink at different temperatures due to their structural transitions, Figure 10. The Ir_2In_8Q compounds have Debye temperatures of 245, 215, and 190 K for the sulfide, selenide, and telluride, respectively, implying that the lattice becomes softer as the chalcogenide atom becomes larger and more polarizable (Figure S8). Ir_2In_8S has a large feature at 230 K, the same temperature that the rods of diffuse scattering disappear and cause the kink in its resistivity. Ir_2In_8Se has a similar feature at 203 K, coincident with the onset of supercell ordering and change in slope in its electrical behavior. And lastly, Ir_2In_8Te has a small kink at ~147 K, also coincident with its supercell ordering and peak in resistivity. All the events in the heat capacity data line up with structural and electronic changes in the materials themselves, but the most curious result is how prominent of a feature Ir_2In_8S had

without showing an abrupt phase transition in the synchrotron x-ray diffraction. As mentioned above, Ir_2In_8S does not have clear supercell ordering like the selenide and telluride analogues, but the dramatic change in x-ray diffuse scattering still causes a notable event in the thermal data.

Conclusion

Liquid indium is an effective reactive flux for the synthesis of the novel tetragonal subchalcogenides Ir_2In_8Q. These materials have essentially intermetallic structures that appear to be stabilized by only a few chalcogen atoms. On cooling to 230 K, the sulfide analogue transitions from a structure with significant rods of diffuse scattering to an undistorted structure with almost no diffuse scattering. Ir_2In_8Se and Ir_2In_8Te have commensurately modulated supercells that appear at 203 and 150 K, respectively, and this ordering disappears (reverting to the original subcell) between 100-110 K in both structures. Charge transport and heat capacity data confirm these features, and their moderate carrier concentrations and high electron mobilities are consistent with the symmetry-protected band crossings near the Fermi level predicted by theoretical calculations. Therefore, Ir_2In_8Se and Ir_2In_8Te are also Dirac semimetal candidates like Ir_2In_8S. We anticipate that other novel subchalcogenide materials could be synthesized from different metal flux media (e.g. Sn, Ga, Pb, etc.), as there is great potential to find materials featuring broad metallic substructures stabilized by chalcogen atoms.

Acknowledgements

Associated Content

Additional DFT calculations, CIF files, crystallographic tables, diffraction images, SEM/EDS, transport, and heat capacity measurements can be found in the supporting information free of charge via the internet at http://pubs.acs.org.

Author Information

Corresponding Author

*E-mail: m-kanatzidis@northwestern.edu

References

1.	Weihrich, R.; Matar, S. F.; Eyert, V.; Rau, F.; Zabel, M.; Andratschke, M.; Anusca, I.; Bernert, T. Structure, ordering, and bonding of half antiperovskites: $PbNi_{3/2}S$ and $BiPd_{3/2}S$. *Prog. Solid State Chem.* **2007,** *35*, 309-327.

2.	Weihrich, R. A., Irina Half Antiperovskites. III. Crystallographic and Electronic Structure Effects in $Sn_{2-x}In_xCo_3S_2$. *Z. Anorg. Allg. Chem.* **2006,** *632*, 1531-1537.

3.	Ruck, M. From the Metal to the Molecule—Ternary Bismuth Subhalides. *Angew. Chem., Int. Ed.* **2001,** *40*, 1182-1193.

4.	Schoop, L. M.; Pielnhofer, F.; Lotsch, B. V. Chemical Principles of Topological Semimetals. *Chem. Mater.* **2018,** *30*, 3155-3176.

5.	Rasche, B.; Isaeva, A.; Ruck, M.; Borisenko, S.; Zabolotnyy, V.; Büchner, B.; Koepernik, K.; Ortix, C.; Richter, M.; van den Brink, J. Stacked topological insulator built from bismuth-based graphene sheet analogues. *Nat. Mater.* **2013,** *12*, 422.

6.	Schnelle, W.; Leithe-Jasper, A.; Rosner, H.; Schappacher, F. M.; Pöttgen, R.; Pielnhofer, F.; Weihrich, R. Ferromagnetic ordering and half-metallic state of $Sn_2Co_3S_2$ with the shandite-type structure. *Phys. Rev. B* **2013,** *88*, 144404.

7.	Sakamoto, T.; Wakeshima, M.; Hinatsu, Y.; Matsuhira, K. Charge-density-wave superconductor $Bi_2Rh_3Se_2$. *Phys. Rev. B* **2007,** *75*, 060503.

8.	Sakamoto, T.; Wakeshima, M.; Hinatsu, Y.; Matsuhira, K. Transport properties in normal-metal $Bi_2Pd_3S_2$ and superconducting $Bi_2Pd_3Se_2$. *Phys. Rev. B* **2008,** *78*, 024509.

9.	Liu, E.; Sun, Y.; Kumar, N.; Muechler, L.; Sun, A.; Jiao, L.; Yang, S.-Y.; Liu, D.; Liang, A.; Xu, Q.; Kroder, J.; Süß, V.; Borrmann, H.; Shekhar, C.; Wang, Z.; Xi, C.; Wang, W.; Schnelle, W.; Wirth, S.; Chen, Y.; Goennenwein, S. T. B.; Felser, C. Giant anomalous Hall effect in a ferromagnetic kagome-lattice semimetal. *Nat. Phys.* **2018,** *14*, 1125-1131.

10.	Wang, Q.; Xu, Y.; Lou, R.; Liu, Z.; Li, M.; Huang, Y.; Shen, D.; Weng, H.; Wang, S.; Lei, H. Large intrinsic anomalous Hall effect in half-metallic ferromagnet $Co_3Sn_2S_2$ with magnetic Weyl fermions. *Nat. Comm.* **2018,** *9*, 3681.

11.	Natarajan, S.; Rao, G. V. S.; Baskaran, R.; Radhakrishnan, T. S. Synthesis and electrical properties of shandite-parkerite phases, $A_2M_3Ch_2$. *J. Less-Common Met.* **1988,** *138*, 215-224.

12.	Ruck, M.; Dubenskyy, V.; Söhnel, T. Structure and Bonding of $Pd@[Bi_{10}]^{4+}$ in the Subbromide $Bi_{14}PdBr_{16}$. *Angew. Chem., Int. Ed.* **2003,** *115*, 3086-3090.

13.	Ruck, M. $Bi_{5.6}Ni_5I$: Eine partiell oxidierte intermetallische Phase mit Kanalstruktur. *Z. Anorg. Allg. Chem.* **1995,** *621*, 2034-2042.

14.	Ruck, M. $Bi_9Rh_2Br_3$, $Bi_9Rh_2I_3$ und $Bi_9Ir_2I_3$ – Eine neue Strukturfamilie quasi-eindimensionaler Metalle. *Z. Anorg. Allg. Chem.* **2000,** *626*, 2449-2456.

15.	Ruck, M. Bi_4RuBr_2 und Bi_4RuI_2: Zwei Varianten einer Kolumnarstruktur mit flächenverknüpften quadratischen $[RuBi_{8/2}]$-Antiprismen. *Z. Anorg. Allg. Chem.* **2004,** *623*, 1583-1590.

16.	Kaiser, M.; Isaeva, A.; Ruck, M. A Metastable Metal with Decagonal Local Symmetry Obtained by Low-Temperature Pseudomorphosis. *Angew. Chem., Int. Ed.* **2011,** *50*, 6178-6180.

17.	Kaiser, M.; Rasche, B.; Ruck, M. The Topochemical Pseudomorphosis of a Chloride into a Bismuthide. *Angew. Chem., Int. Ed.* **2014,** *53*, 3254-3258.

18.	Chen, H. Y.; Tuenge, R. T.; Franzen, H. F. Preparation and crystal structure of $Nb_{14}S_5$. *Inorg. Chem.* **1973,** *12*, 552-555.

19.	Cheng, H. Y.; Franzen, H. F. The crystal structure of Zr_9S_2. *Acta Cryst. B* **1972,** *28*, 1399-1404.

20.	Franzen, H. F. S., J. G. The crystal structure of Ta_6S. *Acta Cryst. B* **1970,** *26*, 125--129.

21.   Yao, X.; Franzen, H. F. Preparation and crystal structure of $Nb_{6.74}$ $Ta_{5.26}S_4$ – a new compound in the ternary system Ta–Nb–S. *Z. Anorg. Allg. Chem.* **1991,** *598*, 353-362.

22.   Yao, X.; Miller, G. J.; Franzen, H. F. Crystal structure and electronic structure of $Nb_xTa_{2-x}S$ (x≈0.95): A new layered compound in ternary Ta-Nb-S system. *J. Alloys. Compd.* **1992,** *183*, 7-17.

23.   Khoury, J. F.; He, J.; Pfluger, J. E.; Hadar, I.; Balasubramanian, M.; Stoumpos, C. C.; Zu, R.; Gopalan, V.; Wolverton, C.; Kanatzidis, M. G. $Ir_6In_{32}S_{21}$, a polar, metal-rich semiconducting subchalcogenide. *Chem. Sci.* **2020,** *11*, 870-878.

24.   Canfield, P. C.; Kong, T.; Kaluarachchi, U. S.; Jo, N. H. Use of frit-disc crucibles for routine and exploratory solution growth of single crystalline samples. *Philos. Mag.* **2016,** *96*, 84-92.

25.   Lin, X.; Bud'ko, S. L.; Canfield, P. C. Development of viable solutions for the synthesis of sulfur bearing single crystals. *Philos. Mag.* **2012,** *92*, 2436-2447.

26.   Zakharova Elena, Y.; Churakov Andrei, V.; Doert, T.; Kuznetsov Alexey, N. $Pd_{17}In_4Se_4$, a Metal-Rich Palladium–Indium Selenide with an Open-Framework Structure. *Eur. J. Inorg. Chem.* **2013,** *2013*, 6164-6169.

27.   Zakharova, E. Y.; Kazakov, S. M.; Isaeva, A. A.; Abakumov, A. M.; Tendeloo, G. V.; Kuznetsov, A. N. Pd_5InSe and Pd_8In_2Se – New metal-rich homological selenides with 2D palladium–indium fragments: Synthesis, structure and bonding. *J. Alloys. Compd.* **2014,** *589*, 48-55.

28.   Franzen, H. F. Structure and bonding in metal-rich compounds: Pnictides, chalcides and halides. *Prog. Solid State Chem.* **1978,** *12*, 1-39.

29.   Kassem, M. A.; Tabata, Y.; Waki, T.; Nakamura, H. Single crystal growth and characterization of kagomé-lattice shandites $Co_3Sn_{2-x}In_xS_2$. *J. Cryst. Growth* **2015,** *426*, 208-213.

30.   Kassem, M. A.; Tabata, Y.; Waki, T.; Nakamura, H. Structure and magnetic properties of flux grown single crystals of $Co_{3-x}Fe_xSn_2S_2$ shandites. *J. Solid State Chem.* **2016,** *233*, 8-13.

31.   Groom, R.; Jacobs, A.; Cepeda, M.; Drummey, R.; Latturner, S. E. $Bi_{13}S_{18}I_2$: (Re)discovery of a Subvalent Bismuth Compound Featuring $[Bi_2]^{4+}$ Dimers Grown in Sulfur/Iodine Flux Mixtures. *Chem. Mater.* **2017,** *29*, 3314-3323.

32.   Kanatzidis, M. G.; Pöttgen, R.; Jeitschko, W. The Metal Flux: A Preparative Tool for the Exploration of Intermetallic Compounds. *Angew. Chem., Int. Ed.* **2005,** *44*, 6996-7023.

33.   Kanatzidis, M. G. Discovery-Synthesis, Design, and Prediction of Chalcogenide Phases. *Inorg. Chem.* **2017,** *56*, 3158-3173.

34.   Khoury, J. F.; Rettie, A. J. E.; Khan, M. A.; Ghimire, N. J.; Robredo, I.; Pfluger, J. E.; Pal, K.; Wolverton, C.; Bergara, A.; Jiang, J. S.; Schoop, L. M.; Vergniory, M. G.; Mitchell, J. F.; Chung, D. Y.; Kanatzidis, M. G. A New Three-Dimensional Subsulfide Ir_2In_8S with Dirac Semimetal Behavior. *J. Am. Chem. Soc.* **2019,** *141*, 19130-19137.

35.   Calta, N. P.; Francisco, M. C.; Malliakas, C. D.; Schlueter, J. A.; Kanatzidis, M. G. Four High-Temperature Ferromagnets in the Hf–Fe–Sn System. *Chem. Mater.* **2014,** *26*, 6827-6837.

36.   SAINT, version 8.38A; Bruker Analytical X-ray Instruments, Inc.: Madison, WI. *SAINT, version 8.38A; Bruker Analytical X-ray Instruments, Inc.: Madison, WI.* **2008**.

37.   Sheldrick, G. M. SHELXTL, version 6.14; Bruker Analytical X-ray Instruments, Inc.: Madison, WI. *SHELXTL, version 6.14; Bruker Analytical X-ray Instruments, Inc.: Madison, WI.* **2003**.

38.   Petříček, V.; Dušek, M.; Palatinus, L. Crystallographic Computing System JANA2006: General features. *Z. Kristallogr. Cryst. Mater.* **2014,** *229*, 345.

39.   Hohenberg, P.; Kohn, W. Inhomogeneous Electron Gas. *Phys. Rev.* **1964,** *136*, B864-B871.

40.   Kohn, W. S., L. J. Self-Consistent Equations Including Exchange and Correlation Effects. *Phys. Rev.* **1965,** *140*, A1133.

41.   Kresse, G.; Furthmüller, J. Efficiency of ab-initio total energy calculations for metals and semiconductors using a plane-wave basis set. *Comput. Mater. Sci.* **1996,** *6*, 15-50.

42.   Kresse, G.; Hafner, J. Ab initio molecular dynamics for open-shell transition metals. *Phys. Rev. B* **1993,** *48*, 13115-13118.

43.   Kresse, G.; Joubert, D. From ultrasoft pseudopotentials to the projector augmented-wave method. *Phys. Rev. B* **1999,** *59*, 1758-1775.

44.   Perdew, J. P.; Burke, K.; Ernzerhof, M. Generalized Gradient Approximation Made Simple. *Phys. Rev. Lett.* **1996,** *77*, 3865-3868.

45.   Hobbs, D.; Kresse, G.; Hafner, J. Fully unconstrained noncollinear magnetism within the projector augmented-wave method. *Phys. Rev. B* **2000,** *62*, 11556-11570.

46.   Krogstad, M. J.; Rosenkranz, S.; Wozniak, J. M.; Jennings, G.; Ruff, J. P. C.; Vaughey, J. T.; Osborn, R. Reciprocal space imaging of ionic correlations in intercalation compounds. *Nat. Mater.* **2020,** *19*, 63-68.

47.   Blankenship, T. V.; Chen, B.; Latturner, S. E. $Ca_{54}In_{13}B_{4-x}H_{23+x}$: A Complex Metal Subhydride Featuring Ionic and Metallic Regions. *Chem. Mater.* **2014,** *26*, 3202-3208.

48.   Schmitt, D. C.; Drake, B. L.; McCandless, G. T.; Chan, J. Y. Targeted Crystal Growth of Rare Earth Intermetallics with Synergistic Magnetic and Electrical Properties: Structural Complexity to Simplicity. *Acc. Chem. Res.* **2015,** *48*, 612-618.

49.   Benavides, K. A.; Oswald, I. W. H.; Chan, J. Y. Casting a Wider Net: Rational Synthesis Design of Low-Dimensional Bulk Materials. *Acc. Chem. Res.* **2018,** *51*, 12-20.

50.   Latturner, S. E. Clusters, Assemble: Growth of Intermetallic Compounds from Metal Flux Reactions. *Acc. Chem. Res.* **2018,** *51*, 40-48.

51.   Canfield, P. C. New materials physics. *Rep. Prog. Phys.* **2019,** *83*, 016501.

52.   Phelan, W. A.; Menard, M. C.; Kangas, M. J.; McCandless, G. T.; Drake, B. L.; Chan, J. Y. Adventures in Crystal Growth: Synthesis and Characterization of Single Crystals of Complex Intermetallic Compounds. *Chem. Mater.* **2012,** *24*, 409-420.

53.   Bugaris, D. E.; Malliakas, C. D.; Han, F.; Calta, N. P.; Sturza, M.; Krogstad, M. J.; Osborn, R.; Rosenkranz, S.; Ruff, J. P. C.; Trimarchi, G.; Bud'ko, S. L.; Balasubramanian, M.; Chung, D. Y.; Kanatzidis, M. G. Charge Density Wave in the New Polymorphs of $RE_2Ru_3Ge_5$ (RE = Pr, Sm, Dy). *J. Am. Chem. Soc.* **2017,** *139*, 4130-4143.

54.   Hoffmann, R. How Chemistry and Physics Meet in the Solid State. *Angew. Chem., Int. Ed.* **1987,** *26*, 846-878.

55.   Bilbao Crystallographic Server, 'Check topological mat', http://www.cryst.ehu.es/cgi-bin/cryst/programs/topological.pl. **2018**.

56.   Liu, Z. K.; Zhou, B.; Zhang, Y.; Wang, Z. J.; Weng, H. M.; Prabhakaran, D.; Mo, S. K.; Shen, Z. X.; Fang, Z.; Dai, X.; Hussain, Z.; Chen, Y. L. Discovery of a Three-Dimensional Topological Dirac Semimetal, Na_3Bi. *Science* **2014,** *343*, 864.

57.   Giannozzi, P.; Andreussi, O.; Brumme, T.; Bunau, O.; Buongiorno Nardelli, M.; Calandra, M.; Car, R.; Cavazzoni, C.; Ceresoli, D.; Cococcioni, M.; Colonna, N.; Carnimeo, I.; Dal Corso, A.; de Gironcoli, S.; Delugas, P.; DiStasio, R. A.; Ferretti, A.; Floris, A.; Fratesi, G.; Fugallo, G.; Gebauer, R.; Gerstmann, U.; Giustino, F.; Gorni, T.; Jia, J.; Kawamura, M.; Ko, H. Y.; Kokalj, A.; Küçükbenli, E.; Lazzeri, M.; Marsili, M.; Marzari, N.; Mauri, F.; Nguyen, N. L.;

Nguyen, H. V.; Otero-de-la-Roza, A.; Paulatto, L.; Poncé, S.; Rocca, D.; Sabatini, R.; Santra, B.; Schlipf, M.; Seitsonen, A. P.; Smogunov, A.; Timrov, I.; Thonhauser, T.; Umari, P.; Vast, N.; Wu, X.; Baroni, S. Advanced capabilities for materials modelling with Quantum ESPRESSO. *J. Phys. Condens. Mat.* **2017,** *29*, 465901.

58.   Giannozzi, P.; Baroni, S.; Bonini, N.; Calandra, M.; Car, R.; Cavazzoni, C.; Ceresoli, D.; Chiarotti, G. L.; Cococcioni, M.; Dabo, I.; Dal Corso, A.; de Gironcoli, S.; Fabris, S.; Fratesi, G.; Gebauer, R.; Gerstmann, U.; Gougoussis, C.; Kokalj, A.; Lazzeri, M.; Martin-Samos, L.; Marzari, N.; Mauri, F.; Mazzarello, R.; Paolini, S.; Pasquarello, A.; Paulatto, L.; Sbraccia, C.; Scandolo, S.; Sclauzero, G.; Seitsonen, A. P.; Smogunov, A.; Umari, P.; Wentzcovitch, R. M. QUANTUM ESPRESSO: a modular and open-source software project for quantum simulations of materials. *J. Phys. Condens. Mat.* **2009,** *21*, 395502.

59.   Maintz, S.; Deringer, V. L.; Tchougréeff, A. L.; Dronskowski, R. LOBSTER: A tool to extract chemical bonding from plane-wave based DFT. *J. Comput. Chem.* **2016,** *37*, 1030-1035.

60.   Chen, H.; Malliakas, C. D.; Narayan, A.; Fang, L.; Chung, D. Y.; Wagner, L. K.; Kwok, W.-K.; Kanatzidis, M. G. Charge Density Wave and Narrow Energy Gap at Room Temperature in 2D $Pb_{3-x}Sb_{1+x}S_4Te_{2-\delta}$ with Square Te Sheets. *J. Am. Chem. Soc.* **2017,** *139*, 11271-11276.

61.   Malliakas, C.; Billinge, S. J. L.; Kim, H. J.; Kanatzidis, M. G. Square Nets of Tellurium: Rare-Earth Dependent Variation in the Charge-Density Wave of $RETe_3$ (RE = Rare-Earth Element). *J. Am. Chem. Soc.* **2005,** *127*, 6510-6511.

62.   Malliakas, C. D.; Iavarone, M.; Fedor, J.; Kanatzidis, M. G. Coexistence and Coupling of Two Distinct Charge Density Waves in Sm_2Te_5. *J. Am. Chem. Soc.* **2008,** *130*, 3310-3312.

63.   Malliakas, C. D.; Kanatzidis, M. G. Divergence in the Behavior of the Charge Density Wave in $RETe_3$ (RE = Rare-Earth Element) with Temperature and RE Element. *J. Am. Chem. Soc.* **2006,** *128*, 12612-12613.

64.   Malliakas, C. D.; Kanatzidis, M. G. Charge Density Waves in the Square Nets of Tellurium of $AMRETe_4$ (A = K, Na; M = Cu, Ag; RE = La, Ce). *J. Am. Chem. Soc.* **2007,** *129*, 10675-10677.

65.   Gooth, J.; Bradlyn, B.; Honnali, S.; Schindler, C.; Kumar, N.; Noky, J.; Qi, Y.; Shekhar, C.; Sun, Y.; Wang, Z.; Bernevig, B. A.; Felser, C. Axionic charge-density wave in the Weyl semimetal $(TaSe_4)_2I$. *Nature* **2019,** *575*, 315-319.

66.   Ghimire, N. J.; Khan, M. A.; Botana, A. S.; Jiang, J. S.; Mitchell, J. F. Anisotropic angular magnetoresistance and Fermi surface topology of the candidate novel topological metal Pd_3Pb. *Phys. Rev. Mater.* **2018,** *2*, 081201.

67.   Miller, S. A.; Witting, I.; Aydemir, U.; Peng, L.; Rettie, A. J. E.; Gorai, P.; Chung, D. Y.; Kanatzidis, M. G.; Grayson, M.; Stevanović, V.; Toberer, E. S.; Snyder, G. J. Polycrystalline $ZrTe_5$ Parametrized as a Narrow-Band-Gap Semiconductor for Thermoelectric Performance. *Phys. Rev. Appl.* **2018,** *9*, 014025.

Table 1. Crystal data and structure refinement for Ir_2In_8Q (Q = S, Se, Te) at 299 K.

Empirical formula	Ir_2In_8S[1]	Ir_2In_8Se[2]	Ir_2In_8Te[3]
Formula weight	1335.02	1381.92	1430.56
Temperature	299 K	299.45 K	299.0 K
Wavelength	0.71073 Å	0.71073 Å	0.71073 Å
Crystal system	Tetragonal	Tetragonal	Tetragonal
Space group	$P4_2/mnm$	$P4_2/mnm$	$P4_2/mnm$
Unit cell dimensions	$a = 9.9200(14)$ Å, $\alpha = 90°$ $b = 9.9200(14)$ Å, $\beta = 90°$ $c = 10.140(2)$ Å, $\gamma = 90°$	$a = 9.9447(12)$ Å, $\alpha = 90°$ $b = 9.9447(12)$ Å, $\beta = 90°$ $c = 10.1091(13)$ Å, $\gamma = 90°$	$a = 10.124(8)$ Å, $\alpha = 90°$ $b = 10.124(8)$ Å, $\beta = 90°$ $c = 10.291(9)$ Å, $\gamma = 90°$
Volume	997.8(3) $Å^3$	999.8(3) $Å^3$	1054.7(19) $Å^3$
Z	4	4	4
Density (calculated)	8.887 g/cm^3	9.181 g/cm^3	9.009 g/cm^3
Absorption coefficient	44.806 mm^{-1}	48.152 mm^{-1}	44.903 mm^{-1}
F(000)	2248	2320	2392
Crystal size	0.163 x 0.107 x 0.084 mm^3	0.143 x 0.06 x 0.044 mm^3	0.14 x 0.03 x 0.025 mm^3
θ range for data collection	2.873 to 29.931°	6.110 to 35.790°	2.822 to 35.504°
Index ranges	-12<=h<=13, -13<=k<=13, -12<=l<=14	-16<=h<=16, -16<=k<=14, -16<=l<=16	-16<=h<=16, -12<=k<=15, -16<=l<=16
Reflections collected	6999	31519	13504
Independent reflections	820 [R_{int} = 0.0304]	1293 [R_{int} = 0.0596]	1332 [R_{int} = 0.0694]
Completeness to θ = 24.949°	100%	97.9%	99.8%
Refinement method	Full-matrix least-squares on F^2	Full-matrix least-squares on F^2	Full-matrix least-squares on F^2
Data / restraints / parameters	820 / 0 / 37	1293 / 0 / 37	1332 / 0 / 37
Goodness-of-fit	1.162	1.187	1.082

Final R indices [I > 2σ(I)]	$R_{obs} = 0.0220$, $wR_{obs} = 0.0463$	$R_{obs} = 0.0285$, $wR_{obs} = 0.0639$	$R_{obs} = 0.0254$, $wR_{obs} = 0.0473$
R indices [all data]	$R_{all} = 0.0224$, $wR_{all} = 0.0465$	$R_{all} = 0.0286$, $wR_{all} = 0.0639$	$R_{all} = 0.0383$, $wR_{all} = 0.0511$
Extinction coefficient	0.00215(7)	0.00222(9)	0.00027(3)
Largest diff. peak and hole	2.946 and -4.687 e·Å^{-3}	5.430 and -5.057 e·Å^{-3}	2.624 and -2.279 e·Å^{-3}

[1]$R = \Sigma||F_o|-|F_c|| / \Sigma|F_o|$, $wR = \{\Sigma[w(|F_o|^2 - |F_c|^2)^2] / \Sigma[w(|F_o|^4)]\}^{1/2}$ and $w=1/[\sigma^2(Fo^2)+34.7316P]$ where $P=(Fo^2+2Fc^2)/3$

[2]$R = \Sigma||F_o|-|F_c|| / \Sigma|F_o|$, $wR = \{\Sigma[w(|F_o|^2 - |F_c|^2)^2] / \Sigma[w(|F_o|^4)]\}^{1/2}$ and $w=1/[\sigma^2(Fo^2)+(0.0114P)^2+38.4561P]$ where $P=(Fo^2+2Fc^2)/3$

[3]$R = \Sigma||F_o|-|F_c|| / \Sigma|F_o|$, $wR = \{\Sigma[w(|F_o|^2 - |F_c|^2)^2] / \Sigma[w(|F_o|^4)]\}^{1/2}$ and $w=1/[\sigma^2(Fo^2)+(0.0160P)^2+4.9304P]$ where $P=(Fo^2+2Fc^2)/3$

Table 2. Bond lengths [Å] for Ir$_2$In$_8$Q at 299 K with estimated standard deviations in parentheses.

Bond	S	Se	Te
Ir(1)-In(1)	2.7532(7)	2.7478(6)	2.8002(19)
Ir(1)-In(2)	2.7993(6)	2.7947(5)	2.827(2)
Ir(1)-In(3)	2.6668(6)	2.6472(5)	2.672(2)
Ir(1)-In(4)	2.6379(6)	2.6230(4)	2.659(2)
Ir(1)-In(5)	2.9016(8)	2.8997(7)	2.9590(19)
In(1)-In(1)	2.6843(19)	2.6806(18)	2.712(3)
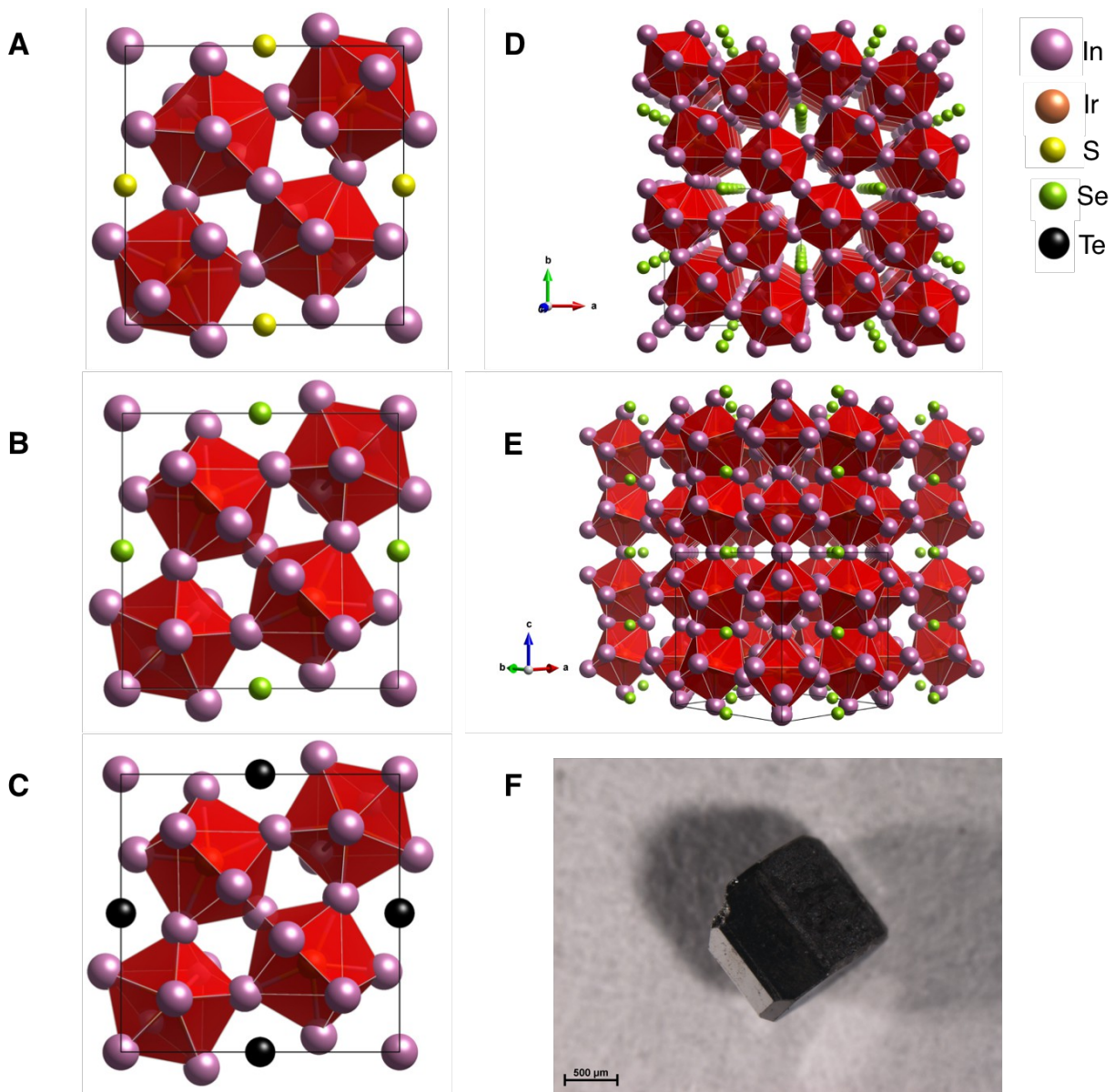
Figure 1: Structure description for Ir$_2$In$_8$Q. (A, B, and C) Individual unit cells of Ir$_2$In$_8$Q (Q = S, Se, Te) along the *c* axis. (D) Extended structure along the *ab* plane, showing the chalcogenide channels along the *c* axis. (E) Extended structure along the *c* axis, showing the alternating corner and edge sharing pattern of the polyhedral. (F) Flux grown crystal of Ir$_2$In$_8$Se, showing the alternating tetragonal faces.
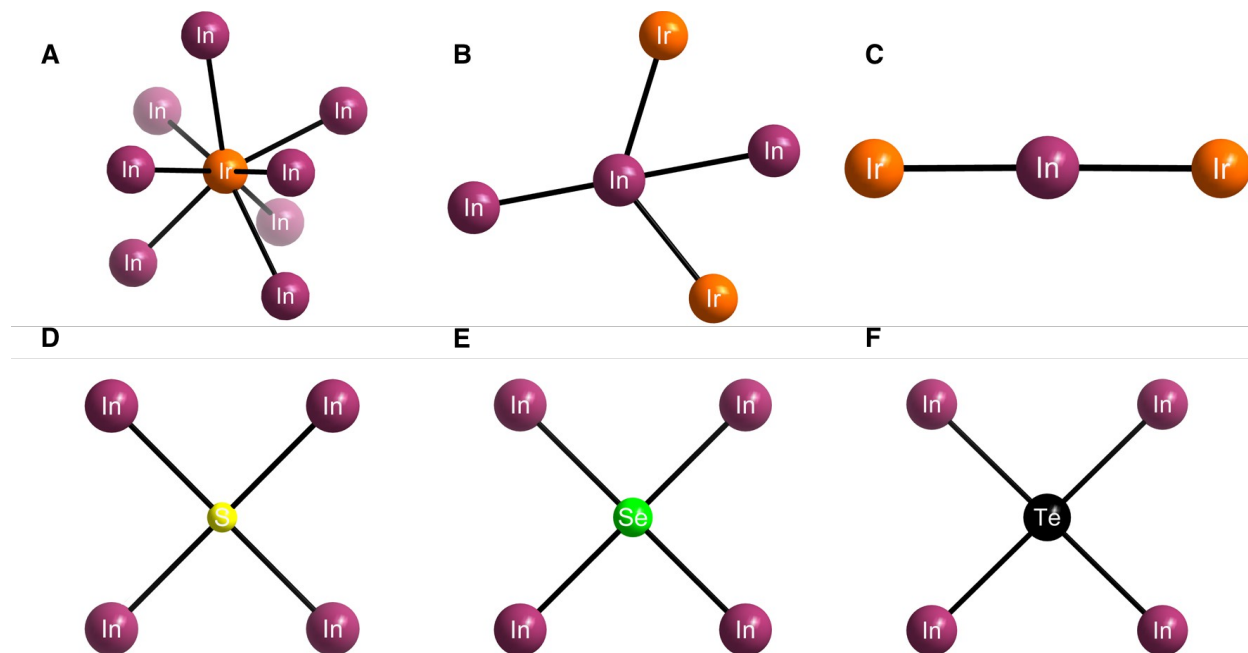
Figure 2: Individual coordination environments for Ir_2In_8Q. (A) $IrIn_8$ distorted bi-capped trigonal prism. (B, C) In coordination environments showing Ir-In and In-In bonds. (D, E, F) Square planar coordination geometry for In-Q, with increasing bond length of 2.8754(6) Å, 2.9394(6) Å, and 3.0982(18) Å for S, Se, and Te, respectively.
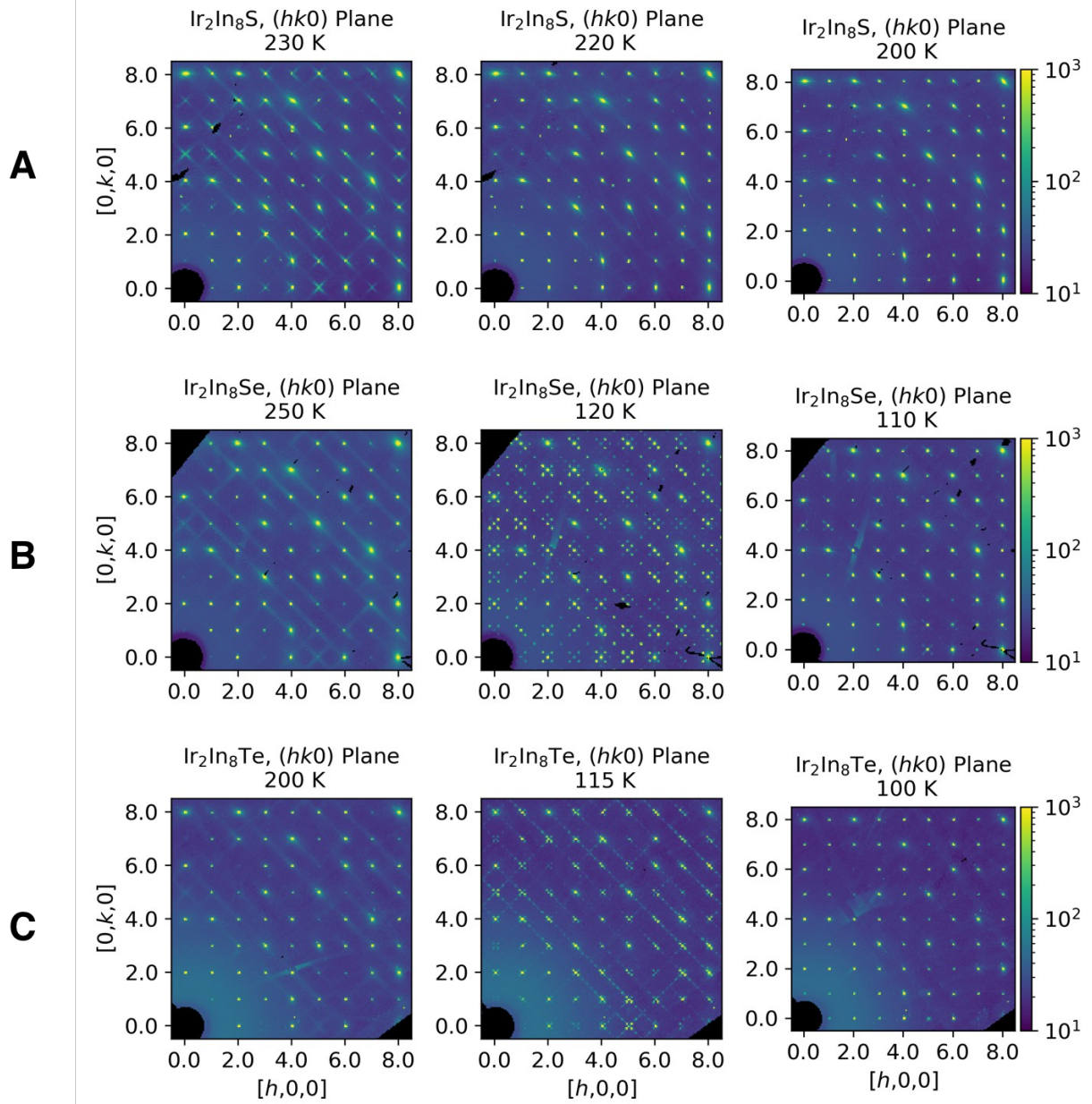
Figure 3: Diffuse scattering images from 6-ID-D at the Advanced Photon Source for for (A) Ir_2In_8S, (B) Ir_2In_8Se, and (C) Ir_2In_8Te. In (A), the diffuse scattering disappears below 230 K. In (B), supercell ordering appears below 203 K and disappears around 110 K. In (C), supercell ordering appears below 150 K and disappears around 100 K.
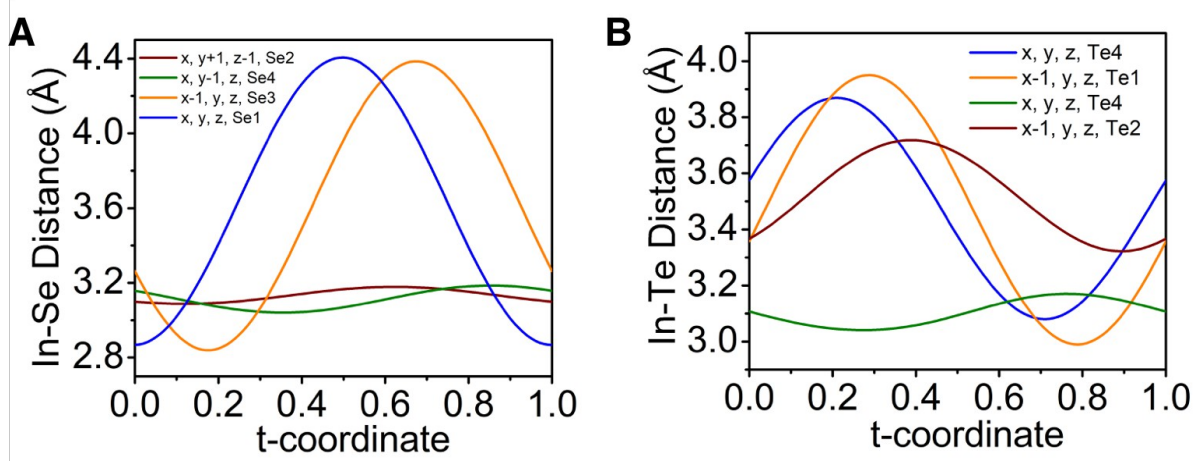
Figure 4: In-Se (A) and In-Te (B) distances in the modulated superstructures of Ir_2In_8Se and Ir_2In_8Te as a function of the t modulation vector. The different colored lines denote symmetry elements for atoms in the $Pm(\alpha\beta0)0$ superspace group.
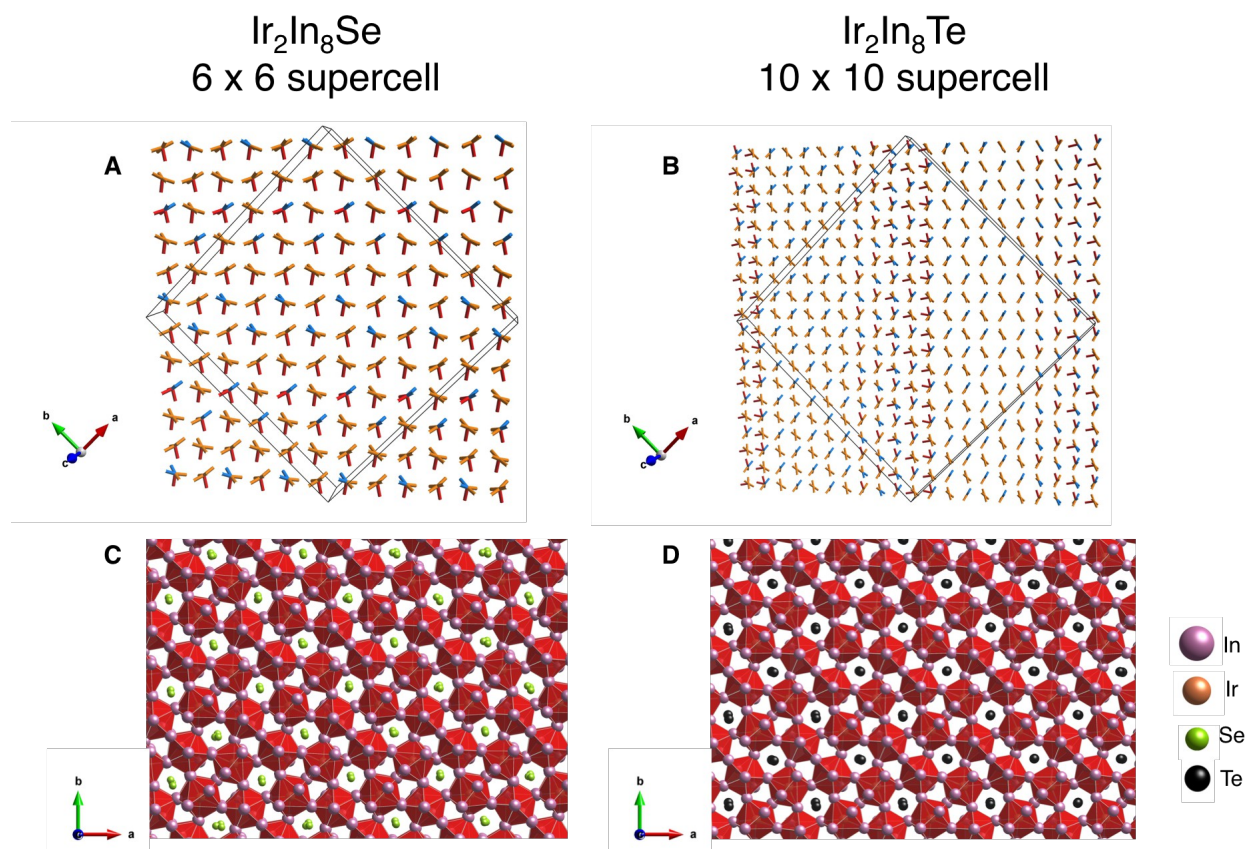
Figure 5: Depiction of In-Q bond alternation in the supercells of (A) Ir_2In_8Se and (B) Ir_2In_8Te. Compressed bonds are in blue, elongated bonds are red, and normal bonds are orange. The elongated axial In-Q bonds increase the coordination number of the chalcogenide atom to 5 or 6 in each structure. Overall modulated structures of (C) Ir_2In_8Se and (D) Ir_2In_8Te clearly show the distortions of the Q atoms both along the *ab* plane and the *c* axis.
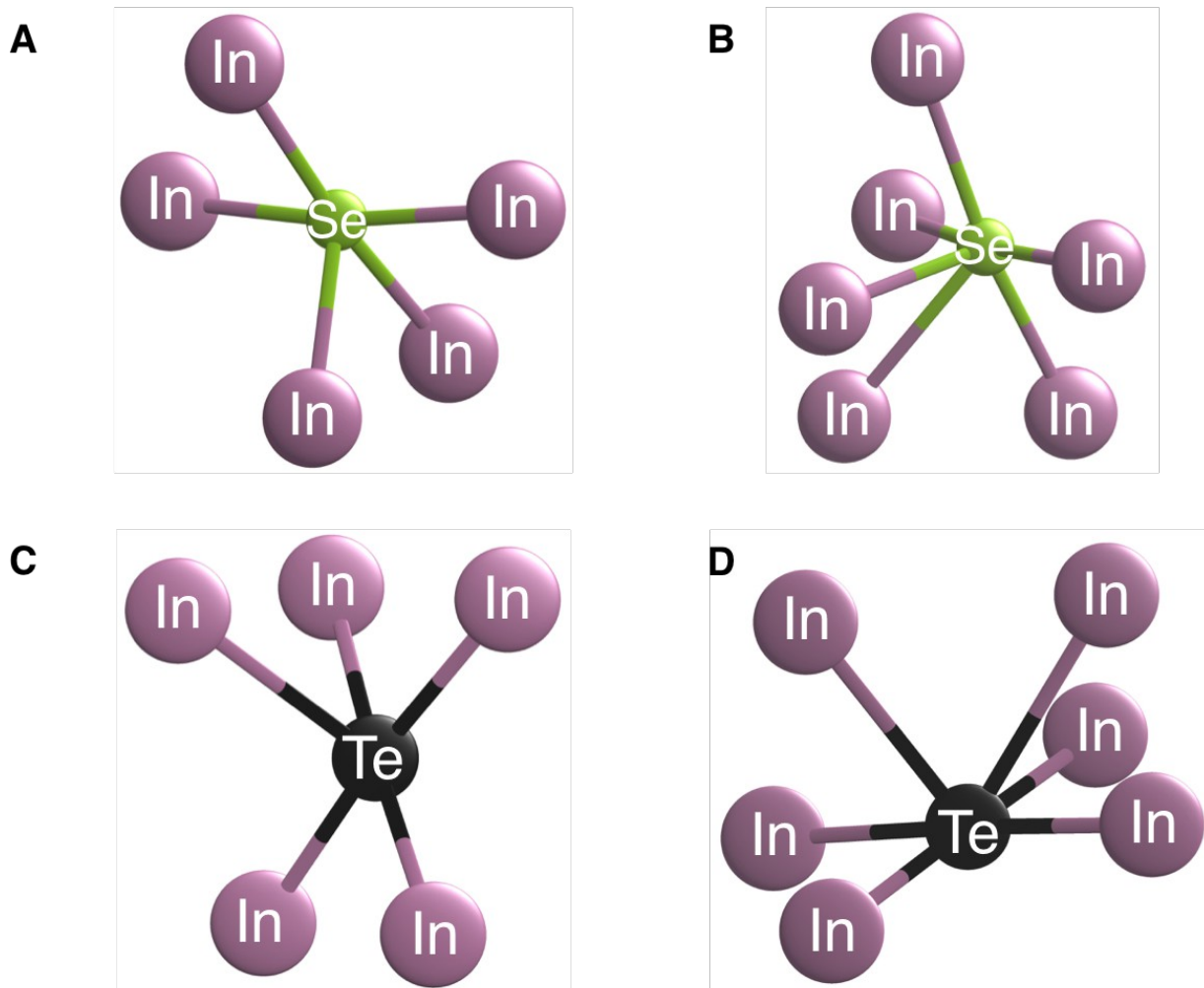
Figure 6: In-Q bond formation in the modulated superstructures of Ir_2In_8Se and Ir_2In_8Te. The subcells show a square planar In-Q coordination geometry, but the supercells show 5 and 6-coordinate In-Se (A, B) and In-Te (C, D). The new In-Q bond lengths vary between ~2.8 – 4 Å, as seen in Figure 4.
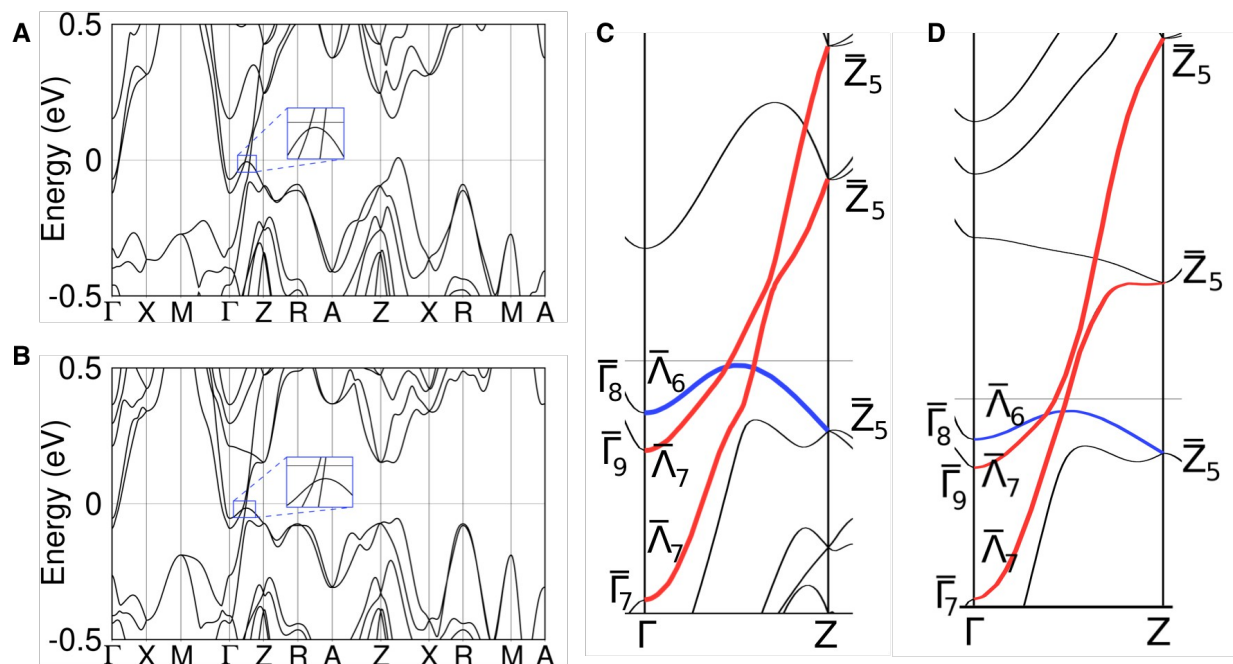
**Figure 7**: Electronic band structures of (A) Ir_2In_8Se and (B) Ir_2In_8Te with insets showing Dirac crossings slightly below the Fermi level. Schematic of symmetry analysis of Ir_2In_8Se (C) and Ir_2In_8Te (D) show the different irreducible representations of the bands, allowing the symmetry-protected band crossings to occur.
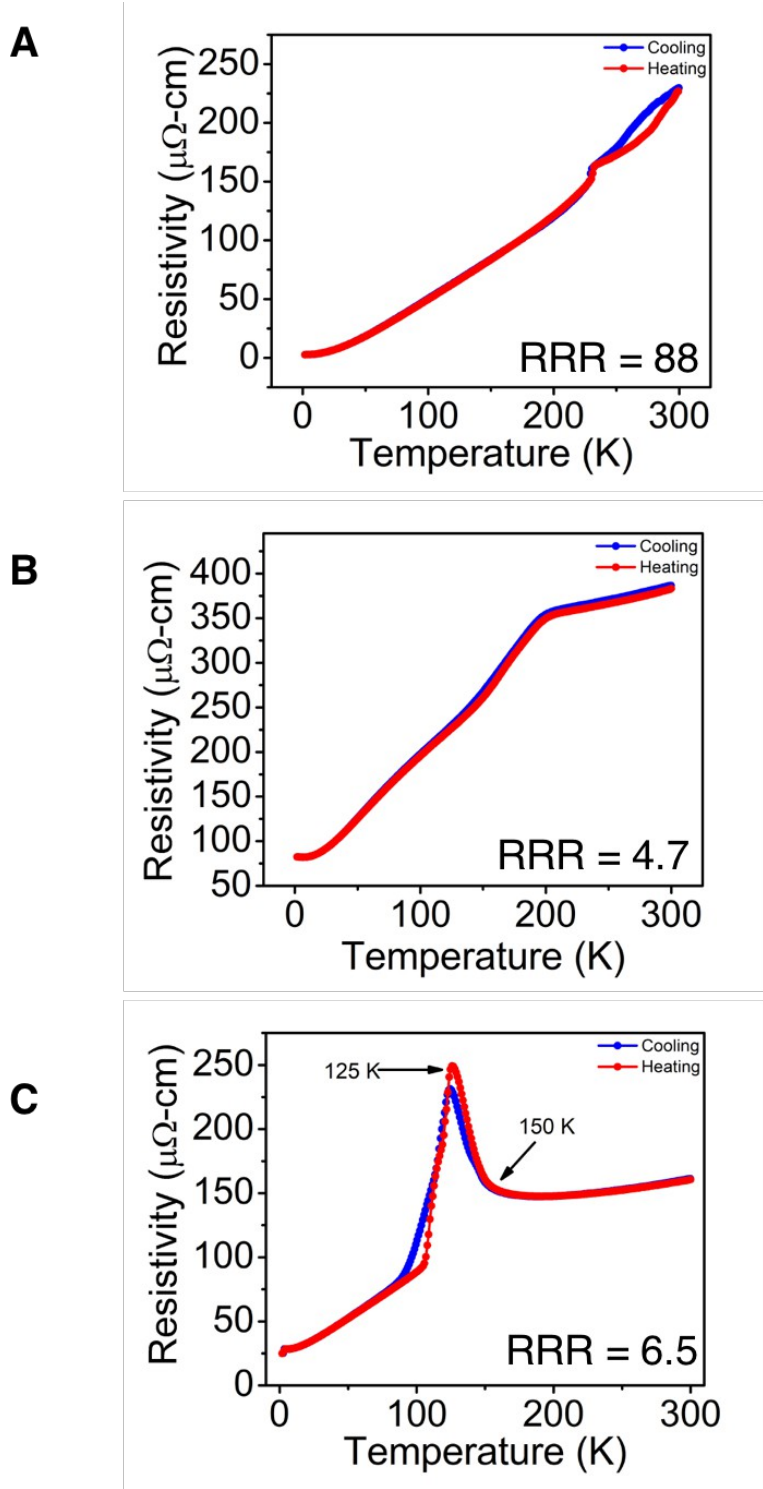
**Figure 8**: Resistivity data (cooling and warming) for (A) Ir_2In_8S, (B) Ir_2In_8Se, and (C) Ir_2In_8Te from 300 K to 1.8 K with listed residual resistivity ratios (RRR, $\rho_{300\ K}/\rho_{1.8\ K}$). Characteristic features include the kink at 230 K in (A), the change in slope at 203 K in (B), and the onset of the peak at 150 K in (C). Changes in diffuse scattering are correlated with the kink in (A), while supercell ordering is responsible for the features in (B) and (C).
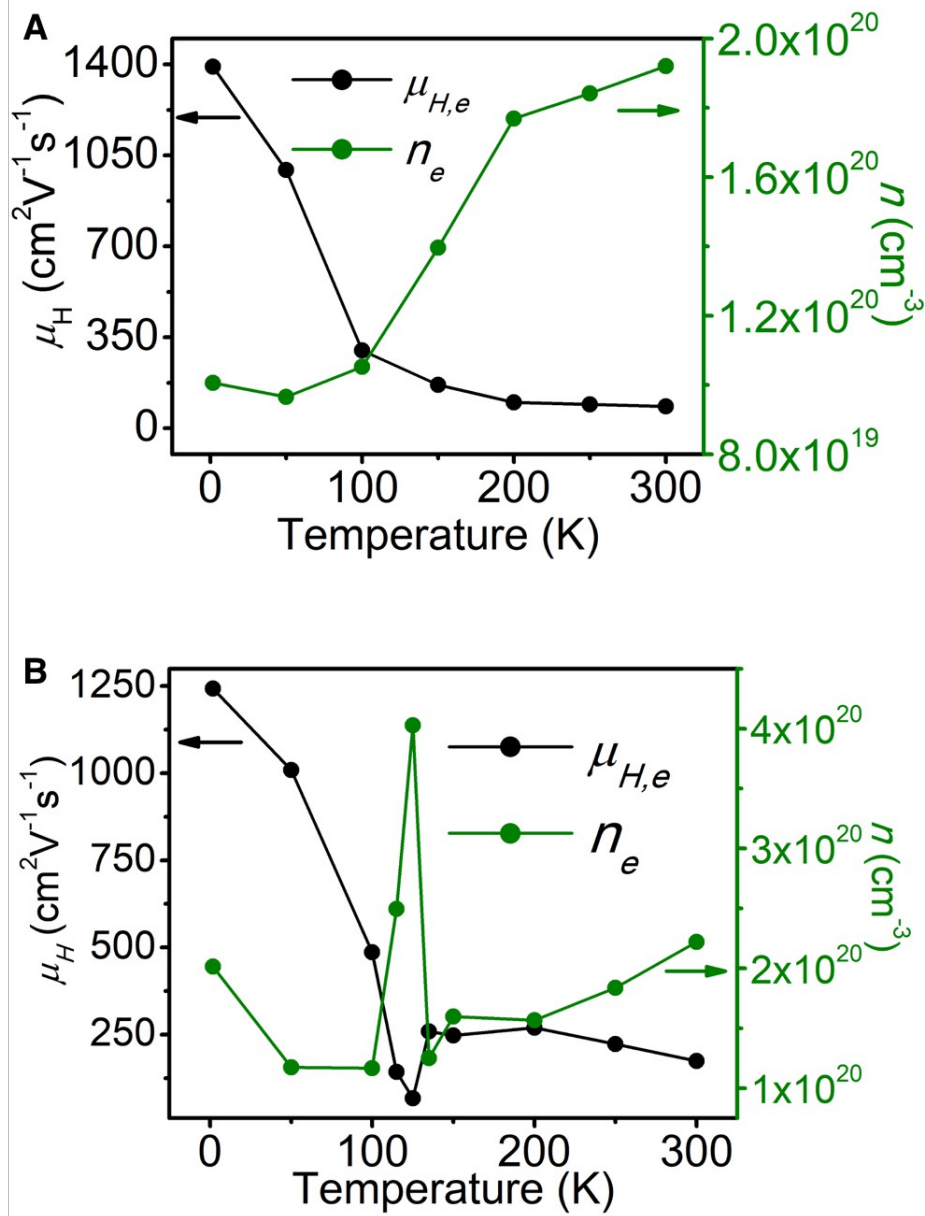
Figure 9: Hall transport data for Ir_2In_8Se (A) and Ir_2In_8Te (B). The carriers are predominantly electron-type with multi-band hole contribution in Ir_2In_8Se below 50 K, with hole values in the supporting information. Both compounds have high mobilities of $\sim$1200 – 1400 $cm^2V^{-1}s^{-1}$ and moderate carrier concentrations of $\sim$2 x 10^{20} cm^{-3}.
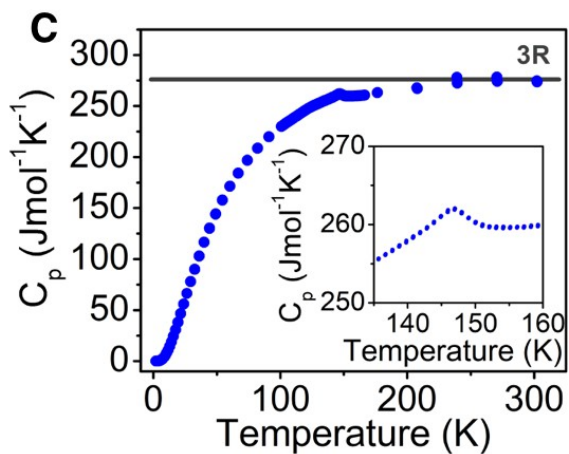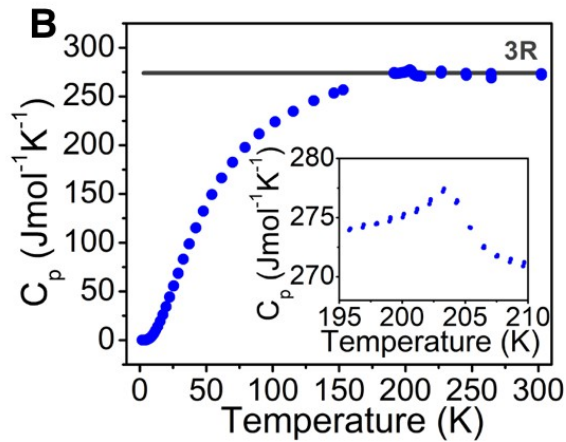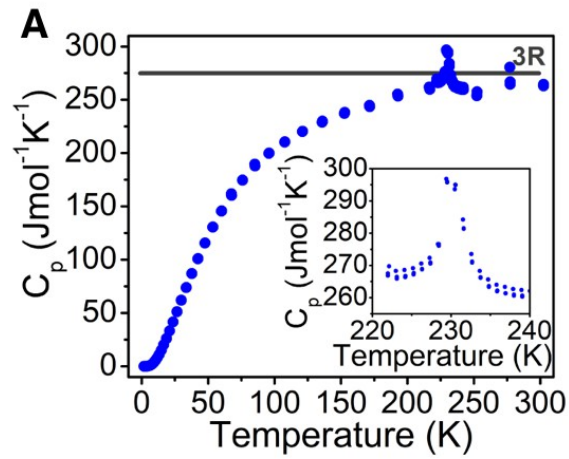
Figure 10: Heat capacity data for (A) Ir_2In_8S, (B) Ir_2In_8Se, and (C) Ir_2In_8Te. There are sharp features at 230 K in (A) and 203 K in (B), and a subtler kink at 150 K in (C). These features correspond to the structural and electrical data that are a result of a change in diffuse scattering in (A) and supercell ordering in (B) and (C).

For Table of Contents Only: